Materials Science & Engineering A 825 (2021) 141930

Contents lists available at ScienceDirect

Materials Science & Engineering A

journal homepage: www.elsevier.com/locate/msea

The complex interaction between microstructural features and crack evolution during cyclic testing in heat-treated Al–Si–Mg–Cu cast alloys

Toni Bogdanoff [a,*], Lucia Lattanzi [a,b], Mattia Merlin [b], Ehsan Ghassemali [a], Anders E.W. Jarfors [a], Salem Seifeddine [a]

[a] Department of Materials and Manufacturing, Jönköping University, Box 1026, 55111, Jönköping, Sweden
[b] Department of Engineering, University of Ferrara, Via Giuseppe Saragat 1, 44122 Ferrara, Italy

ARTICLE INFO

Keywords:
Aluminium alloys
Electron microscopy
Characterisation
Casting methods
Fatigue

ABSTRACT

The study aimed to investigate crack initiation and propagation at the micro-scale in heat-treated Al–7Si–Mg cast alloys with different copper (Cu) contents. In-situ cyclic testing in a scanning electron microscope coupled with electron back-scattered diffraction and digital image correlation was used to evaluate the complex interaction between the crack path and the microstructural features. The three-nearest-neighbour distance of secondary particles was a new tool to describe the crack propagation in the alloys. The amount of Cu retained in the α-Al matrix after heat treatment increased with the Cu content in the alloy and enhanced the strength with a slight decrease in elongation. During cyclic testing, the two-dimensional (2D) crack path appeared with a mixed propagation, both trans- and inter-granular, regardless of the Cu content of the alloy. On fracture surfaces, multiple crack initiation points were detected along the thickness of the samples. The debonding of silicon (Si) particles took place during crack propagation in the Cu-free alloy, while cracking of Si particles and intermetallic phases occurred in the alloy with 3.2 wt% Cu. Three-dimensional tomography using focused ion beam revealed that the improved strength of the α-Al matrix changes the number of cracked particles ahead of the propagating crack with Cu concentration above 1.5 wt%.

1. Introduction

Nowadays, the automotive sector strives for lightweight solutions for reducing gas emissions and fuel consumption [1,2]. Besides, the components of electric vehicles must meet additional requirements regarding reduced weight and optimised mechanical performance. For these reasons, it is crucial to perfectly match the selection of materials to the operational life of components [3]. Hypoeutectic Al–Si cast alloys are a valid candidate for fulfilling these requirements, particularly with the right combination of alloying elements, such as magnesium (Mg) and copper (Cu), and post solidification treatments. The addition of Mg and Cu combined with proper heat treatment provides a good compromise between the ductility of Al–Si–Mg alloys and the strength of Al–Si–Cu systems [4–6]. For this reason, over the last two decades, the literature has addressed the addition of Cu to Al–Si–Mg cast alloys for both as-cast [4–7] and heat-treated conditions to obtain high strength [8–19].

The T6 heat treatment is typically applied to Al–Si–Mg and Al–Si–Cu–Mg alloys and consists of solution treatment, quenching, and ageing. These steps lead to dispersed precipitates that hinder dislocation movements and improve the strength of the material. In Al–Si–Mg alloys, the precipitation sequence during ageing results in an incoherent β-Mg_2Si phase [17]. The addition of Cu changes the precipitation sequence of the alloy, inducing Cu-based precipitates, as reported in the literature [12–14]. For a Cu content greater than 1.5 wt%, the incoherent θ-Al_2Cu phase ends the precipitation sequence and suppresses the β-Mg_2Si phase [17]. The strength improvement is due to a sufficient number of precipitates of appropriate size and spacing. Peak ageing generally occurs within the transition from coherent to semi-coherent precipitates when the optimal number density combined with optimal precipitate spacing is reached [18]. Natural ageing before artificial ageing is beneficial for Al–Si–Mg alloys because it promotes a microstructure with a lower number density of coarser particles compared to the directly artificially aged alloy [18,19].

As a consequence of heat treatment, the addition of Cu improves the

* Corresponding author.
E-mail addresses: toni.bogdanoff@ju.se (T. Bogdanoff), lucia.lattanzi@ju.se (L. Lattanzi), mattia.merlin@unife.it (M. Merlin), ehsan.ghassemali@ju.se (E. Ghassemali), anders.jarfors@ju.se (A.E.W. Jarfors), salem.seifeddine@ju.se (S. Seifeddine).

https://doi.org/10.1016/j.msea.2021.141930
Received 23 February 2021; Received in revised form 12 August 2021; Accepted 17 August 2021
Available online 20 August 2021
0921-5093/© 2021 The Authors. Published by Elsevier B.V. This is an open access article under the CC BY license (http://creativecommons.org/licenses/by/4.0/).

Yield Strength (YS) and Ultimate Tensile Strength (UTS) of Al–Si–Mg alloys. Caceres et al. [16] investigated the influence of Si, Cu, and Mg on the tensile properties of heat-treated Al–Si–Mg–Cu systems. They concluded that to achieve the optimal mechanical response, Cu content should be limited to 3 wt% when Mg content is above 1 wt%. Zheng et al. [15] investigated Al–6Si–Cu–Mg alloys with Cu/Mg ratios from 1 to 4. They reported that the precipitation sequence depends on the Cu content and the Cu/Mg ratio: a low-ratio alloy tends to preferentially form the precursor of β precipitates, whereas a high-ratio alloy will lead to the formation of Q and θ precursors. A higher Cu/Mg ratio by increasing Cu content improves both strength and elongation.

The effect of T6 heat treatment also influences the fatigue response of the material. In particular, crack propagation is characterised by significantly more branching and crack deflection compared to the as-cast condition due to crack-tip shielding and lower crack growth rates [20]. For this reason, Lados et al. [21–23] have been focusing their attention on the influence of microstructural features on long and small fatigue crack growth in heat-treated Al–Si–Mg alloys. About the α-Al matrix strength, they reported that the crack growth rate is higher for naturally-aged samples than for T6 ones in upper Region II and lower Region III of the Paris curve. On the other hand, in upper Region III, naturally-aged material showed improved fatigue crack growth resistance due to the ductile tearing in the α-Al matrix.

From this background, an in-depth understanding of crack initiation and propagation on the microstructural scale is crucial for developing high-performance alloys, especially for the transportation sector. In addition, structural components like suspension systems must withstand dynamic loading [24–26], and it is crucial to assess the role of the heat-treated microstructure in either promoting or shielding crack propagation.

The present work aimed to identify the microstructural features that significantly influence the crack initiation and propagation of a Cu-added Al–7Si–Mg alloy after T6 heat treatment. The Cu additions were selected for specific reasons: 0.5 wt% is the Cu content in the EN-AC 45500 alloy, 1.5 wt% is the content for the best strength-ductility compromise [4–6,27], 3 wt% is the Cu content in the EN-AC 46500 alloy. Directional solidification enabled the control of cooling rate and grain size with a limited number of defects [5] to focus specifically on the role of Cu-related features. In-situ cyclic testing using a Scanning Electron Microscope (SEM) and Digital Image Correlation (DIC) highlighted the interaction between crack development and microstructural features. The distance between Si particles and Cu-rich phases, quantified with the three-nearest neighbour (3NN) distance, is an important parameter to consider because it significantly affects the crack propagation of these alloys. Tortuosity is an additional tool to describe the crack path numerically. The results from our previous work on the same alloys before heat treatment [28] were the starting point to comprehensively understand the influence of heat treatment in the present study. Besides, previous work [28] shed light on the role of Cu-related microstructural features, highlighting that Cu is beneficial for material strengthening up to a threshold limit for ductility. The results lead to assessing the mechanical response of the heat-treated alloys, typically employed in service condition of structural cast components. To the best of the knowledge of the authors, no similar detailed investigations have been performed to evaluate the crack propagation at the microscale level on the heat-treated Cu-added Al–Si–Mg alloys during cyclic loading. This understanding will benefit the design of structural components in vehicles with optimised performance.

2. Experimental procedure

2.1. Preparation and characterisation of alloys

Pure Al ingots, pure Si, and an Al–50Mg master alloy were melted in a boron nitride-coated crucible to prepare four Al–Si–Mg alloys with different Cu concentrations. Cu contents were obtained with the addition of an Al–50Cu master alloy. After the completion of melting, grain refiner (Al–5Ti–1B) and modifier (Al–10Sr) master alloys were also added to achieve the intended contents of 650–700 ppm of titanium (Ti) and 200–250 ppm of strontium (Sr). Table 1 presents the chemical composition of each alloy, which was evaluated with an optical emission spectrometer (Spectromaxx CCD LMXM3, Spectro Analytical Instruments).

Cylindrical rods (length 150 mm, diameter 9 mm) were cast, remelted, and drawn from a directional solidification furnace raising at ~6 mm/s. This technique produces a low-defect material because the solidification front pushes oxides and porosities towards the top of the samples [5]. It also enabled a targeted average Secondary Dendrite Arm Spacing (SDAS) of 10 μm and targeted Average Grain Size (AGS) of 90 μm. Solution treatment was performed at 495 °C for 1 h, followed by quenching in water at 50 °C. After 24 h of natural ageing, artificial ageing followed at 210 °C for 1.5 h. The parameters for the T6 heat treatment were selected according to the work of Sjölander and Seifeddine [29]. The heat-treatment parameters were selected to reach the peak strength of the Cu-added alloys and also applied to the Cu-free alloy, considered as a reference alloy.

Electron Back-Scattered Diffraction (EBSD - Hikari Plus, Eden Instruments), Wavelength Dispersive X-ray Spectroscopy (WDS - Texs HP, Edax), and Energy Dispersive X-ray Spectroscopy (EDS - Octane Pro, Edax) were employed in a SEM (Lyra3, Tescan) to determine the AGS, quantify the element composition in the primary α-Al matrix, and identify the secondary phases, respectively. Optical microscope (GX71, Olympus) and SEM (EVO MA15, Zeiss) were employed for microstructural investigations. Quantitative image analysis (ImageJ) on Si and Cu-containing particles was conducted to measure the 3NN distance, area, aspect ratio ($Feret_{min}/Feret_{max}$) and circularity ($4*\pi*area/perimeter^2$), as defined by the ISO 9276–6:2008 standard. The 3NN distance, as developed in Ref. [30], of secondary particles was measured using the x and y coordinates of each particle centroid. The field of view (FOV) in the micrographs constituted the reference system for the coordinates. Crack tortuosity was applied to describe the crack propagation, which is a dimensionless ratio between the actual crack length and its equivalent straight path. It quantifies the crack path deviation from linearity: it is equal to 1 for perfectly linear paths and higher than 1 for tortuous paths. SDAS and AGS were evaluated according to Method D from Vandersluis et al. [31] and the Heyn's linear intercept method from the ASTM E112 standard, respectively.

The influence of Cu on the α-Al matrix strength was also assessed using Vickers microhardness (HV0.01) measurements (FM-110, Future Tech Corp). Tensile test specimens with a gauge length of 50 mm and a diameter of 6 mm were machined from the heat-treated rods. Tensile testing (Z100, Zwick Roell) was carried out at room temperature, following the ASTM E8 standard, with a constant cross-head speed of 0.5 mm/min. A minimum of four samples was tested for each condition with a clip-on extensometer to measure the strain.

2.2. In-situ cyclic testing and related techniques

Miniature Compact-Tension (CT) samples were cut using electric discharge machining with a 0.25 mm wire. The miniaturised CT sample dimensions, shown in Fig. 1a, were designed based on the ASTM E647-00 standard guidelines.

The FOV size was 300 μm × 300 μm, and it comprehended the notch

Table 1
Nominal chemical composition [wt.%] of the investigated alloys.

Alloy	Si	Mg	Cu	Fe	Ti	Sr	Al
Cu 0	6.80	0.38	0.00	0.10	0.07	0.03	Balance
Cu 0.5	7.01	0.37	0.51	0.09	0.07	0.02	Balance
Cu 1.5	7.14	0.38	1.61	0.09	0.07	0.02	Balance
Cu 3.0	6.98	0.36	3.23	0.17	0.08	0.02	Balance

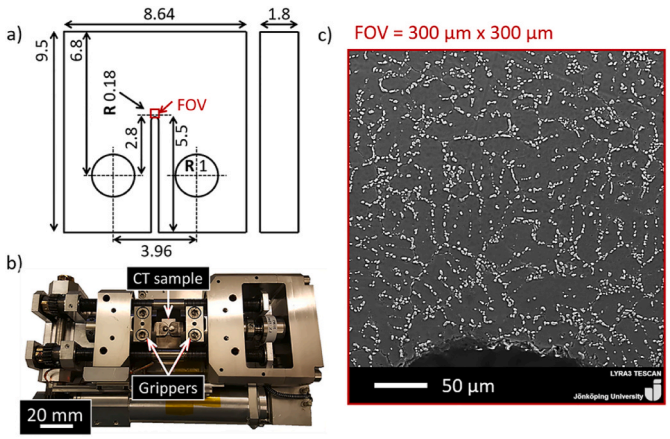

Fig. 1. a) Dimensions of the Compact-Tension (CT) sample in mm; b) miniature stage for in-situ cyclic tests; c) Field Of View (FOV) of the sample, showing the Silicon (Si) particles that formed the random pattern for subsequent Digital Image Correlation (DIC). (For interpretation of the references to colour in this figure legend, the reader is referred to the Web version of this article.)

tip to investigate local strain development (Fig. 1c). CT samples were electropolished (15 V for 5 s) to produce a mirror finish for SEM observations, EBSD, and DIC. EBSD maps were acquired before and after the in-situ fatigue tests to analyse the interaction between the crack and grain boundaries. In-situ cyclic tests were performed on a tensile/compression module (Kammrath & Weiss) (Fig. 1b) inside a SEM (Lyra3, Tescan) at room temperature. Before cyclic loading, the monotonic tension load to failure of the CT samples showed that the critical stress intensity factor (Kc) increased with Cu content, as is shown in Table 2. The selected $\Delta K = (1 - R)*K_{max}$ is reported in Table 2 for each alloy, with a constant load ratio (R) of 0.2. The selected K_{max} value is 70% of the Kc for each alloy. The speed of loading was 8 µm/s (~0.1 Hz). Two samples of each alloy were tested, and one extra sample of Alloys Cu 0 and Cu 3.0 was investigated for Focused Ion Beam (FIB) slicing.

DIC was performed with the MatchID commercial software (MatchID Nv) to obtain the strain distribution on the deformed micrographs at different cycles. Eutectic Si particles (Fig. 1c) constituted the natural random pattern for DIC, representing a time- and cost-saving alternative to artificial patterns. Table 3 presents the correlation parameters used for the DIC analysis, following the work of Kasvayee et al. [32]. The resolution of the strain distribution enabled the evaluation of the role of grain boundaries in strain development.

Three-Dimensional (3D) tomography using FIB (Cobra, Orsay Physics)-SEM (Lyra3, Tescan) was used to observe the crack path in detail, providing more information than was obtained using Two-Dimensional (2D) investigations. A location ahead of the propagating crack was selected in an unloaded state, and a rough milling of ~1.7 µA at 30 kV made a trench around the Area Of Interest (AOI). Fine polishing and slicing of the AOI were conducted using a FIB current of ~30 nA at 30 keV. The thickness of each slice was 120 nm and captured around 300 SEM images at 5 keV using a high-sensitivity in-beam back-scattered electrons detector.

Table 2
Parameters of cyclic testing.

Alloy	K_C [MPa*√m]	Preload [N]	Pmax [N]	Kmax [MPa*√m]	ΔK [MPa*√m]
Cu 0	39.3	364	312	27.4	21.9
Cu 0.5	44.4	410	354	31.1	24.9
Cu 1.5	47.6	441	379	33.3	26.7
Cu 3.0	50.2	463	400	35.2	28.1

Table 3
Correlation parameters used for digital image correlation (DIC).

Parameter	Value
Pixel size [µm]	0.24
SS = Subset size [pixel]	111
ST = Step size [pixel]	11
Correlation criterion	Zero-normalised sum of squared differences
Shape function	Quadratic
Interpolation function	Bi-cubic polynomial
Displacement standard deviation [pixel]	0.1
SW = Strain window size [pixels]	15
SSR = Strain spatial resolution [pixels] SSR = SS + [(SW- 1)*ST]	173

3. Results and discussion

3.1. Microstructural characterisation

The microstructural investigations of the alloys confirmed that the SDAS and AGS were in the 8.8–11 µm and 82–107 µm ranges, respectively. These parameters validate that all alloys were in the same conditions of grain refinement and solidification. The morphology of Si particles plays a crucial role in the mechanical properties of the alloys, and the solution treatment spheroidised and coarsened them. Fig. 2a compares the values of the area, aspect ratio and circularity of Si particles in all the considered alloys.

The average area of the Si particles was significantly larger than in previous work [28], up to seven times due to coarsening during heat treatment. This evolution is evident from comparing the microstructure of Alloy Cu 3.0 before (Fig. 2b) and after heat treatment (Fig. 2c). On the other hand, aspect ratio and circularity were not altered much by heat treatment, as the modified Si particles already had a round morphology in the as-cast condition [28].

The Si and Mg content in the centre of the primary dendrites measured by WDS showed a slight decrease with the addition of Cu: Si changed from 0.94 ± 0.03 to 0.84 ± 0.01 wt%, Mg went from 0.32 ± 0.01 to 0.27 ± 0.01 wt%. The latter WDS measurements confirmed the dissolution of the Mg_2Si phase in the Alloys Cu 0 and Cu 0.5. Fig. 3b presents the Cu content in the α-Al dendrites measured by WDS. The result for Alloy Cu 0.5 is 0.52 wt%, and the comparison with Table 1 shows that Cu-based phases were completely dissolved. However, traces of the Q-$Al_5Mg_8Cu_2Si_6$ phase were still present after heat treatment in alloys with Cu contents of 1.5 wt% and 3.2 wt% (the latter depicted in Fig. 3a), while θ-phase was dissolved. The calculated Cu content in the remaining Q-phase (identified by EDS) summed with the Cu content in the primary α-Al matrix (measured using WDS) agree with the overall Cu content in each alloy (Fig. 3b). This phenomenon occurred because the solution treatment at 495 °C for 1 h did not entirely dissolve the Q-phase. The complete dissolution of the Q phases requires either a two-step solution treatment, as presented by Wang et al. [33] and Toschi [34], or a treatment period longer than 1 h [35,36].

The heat treatment also influenced the relative distance between the secondary phases, i.e. eutectic Si particles and Cu-based phases. Fig. 4 summarise the 3NN distance measurements.

Si particles (Fig. 4a) presented an average 3NN distance of 0.63 µm before heat treatment, independent of Cu content. After heat treatment, the distance was in the 1.40–2.32 µm range due to the coarsening effect. On the other hand, the 3NN distance of Q phases (Fig. 4b) decreased from 3.55 µm in Alloy Cu 0.5–0.78 µm in Alloy Cu 3.0 before heat treatment. This decreasing trend mirrored the more significant number of intermetallic particles, resulting in a closer distance to each other. After heat treatment, the decreasing trend shifted to higher values, from 9.10 µm in Alloy Cu 0.5–4.10 µm in Alloy Cu 3.0 due to the partial dissolution of Q phases.

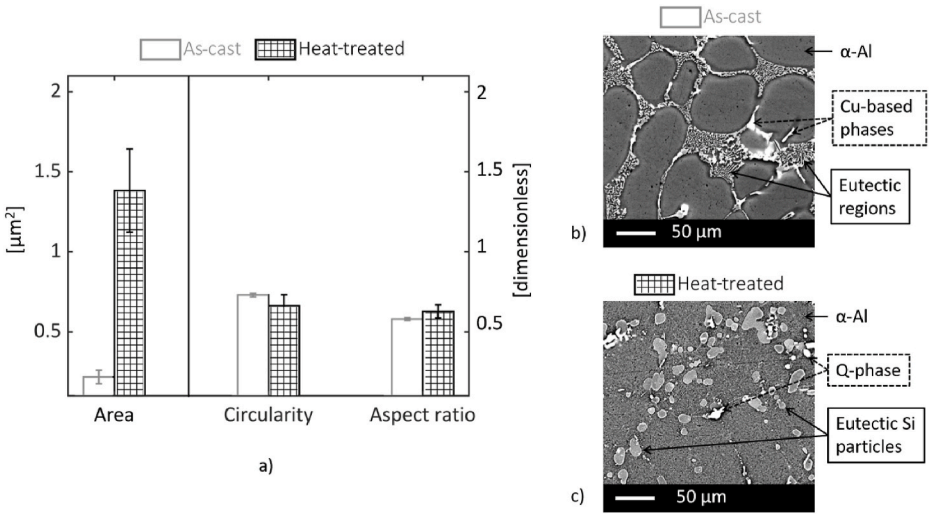

Fig. 2. Evolution of the eutectic Si particles after heat treatment: a) values of the area (μm^2, left y-axis) and geometrical parameters (dimensionless, right y-axis) of Si particles in the alloys; examples of microstructure for Alloy Cu 3.0 b) before and c) after heat treatment. As-cast data are reported from previous work [28].

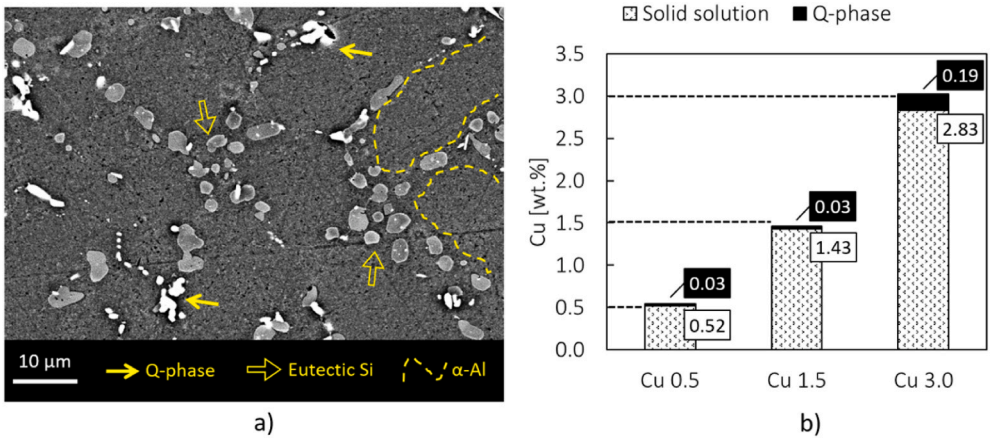

Fig. 3. a) Microstructure of heat-treated Alloy Cu 3.0; b) Cu content in solid solution and undissolved Q-phase. The latter is calculated according to the theoretical Cu content in the Q-$Al_5Mg_8Cu_2Si_6$ phase (~20 wt%). Dashed lines represent the overall Cu content in each alloy.

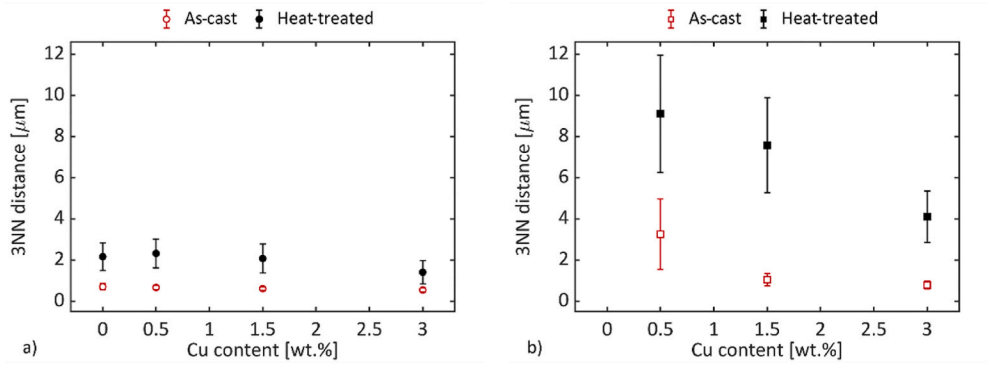

Fig. 4. Three-Nearest-Neighbour (3NN) distance of particles: a) eutectic Si; b) Q phase. The error bars represent the standard deviation.

3.2. Static mechanical properties

The mechanical properties showed an improvement in YS (Fig. 5a) and UTS (Fig. 5b) and a decrease in elongation (Fig. 5c) with increasing Cu concentration. The YS improved from 3 to 35% as Cu increased from 0.5 to 3.2 wt%, while UTS increased from 10 to 47%. However, the reduction in elongation was negligible compared to the reduction in previous work [28], indicating the detrimental role of the Cu-rich phases. Nevertheless, the heat treatment was beneficial, particularly for alloys with Cu contents of greater than 1.5 wt%, and in general, it homogenised the elongation response of the alloys.

The enhancement in YS and UTS was related to the precipitation

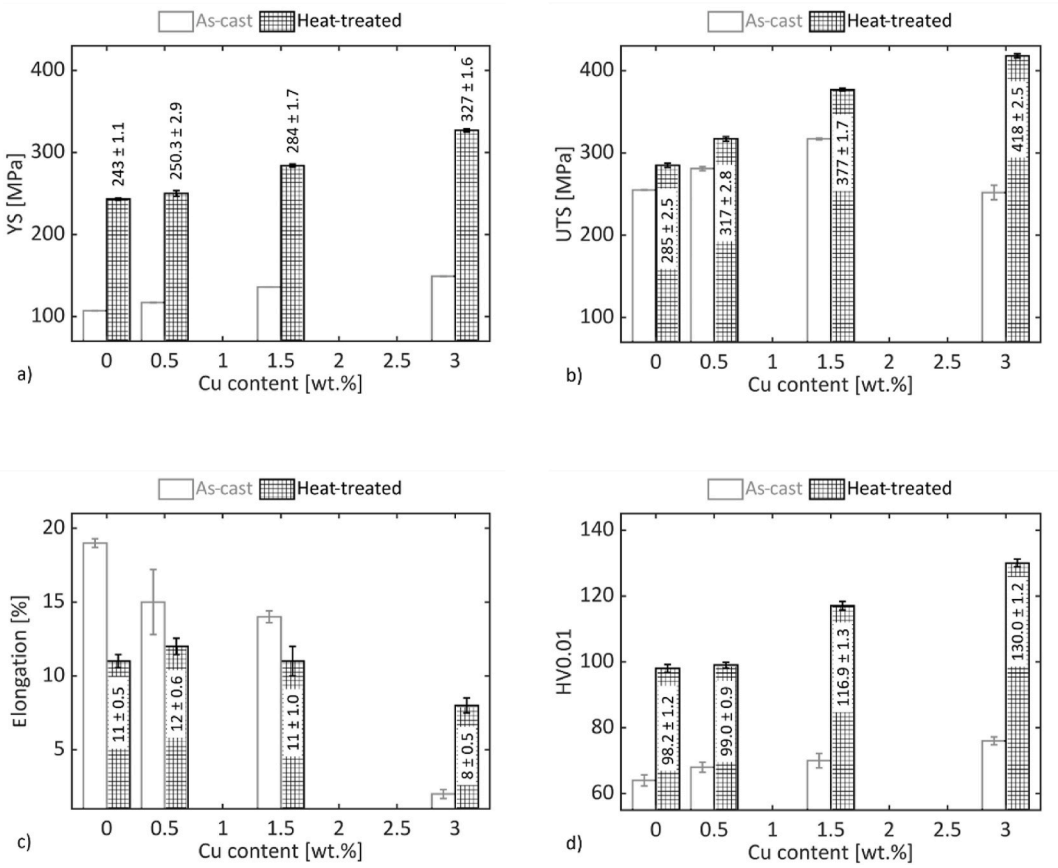

Fig. 5. Mechanical properties of the heat-treated alloys: a) Yield Strength (YS); b) Ultimate Tensile Strength (UTS); c) percentage elongation; d) Vickers microhardness (HV0.01) of the primary α-Al matrix. The as-cast values from previous work [28] are depicted for direct comparison.

hardening, also reported by Zheng et al. [15]. Comparing the increasing trend of YS and UTS after heat treatment with the WDS measurements (Fig. 3b), it is clear that the strengthening role of the Cu retained in the primary α-Al matrix was coupled with the partial dissolution of the Q phases and the total dissolution of the θ phases during heat treatment. The percentage increment in YS (Fig. 5a) mirrored the percentage improvement in HV0.01 of the primary α-Al matrix (Fig. 5d), from 1 to 36%, as Cu increased from 0.5 to 3.2 wt%. Fig. 5d shows that the hardness of the α-Al matrix varied in the range of 98 ÷ 130 HV0.01 for the heat-treated alloys, and the strengthening after heat treatment was related to the Cu retained in the α-Al matrix (Fig. 3b).

The limited variation of Si morphology (aspect ratio and circularity in Fig. 2a) and 3NN distance (Fig. 4a) after heat treatment was common to all of the alloys, and it underlines that the mechanical response was primarily affected by the Cu-based phases in this study. The decreasing 3NN distance between Q phases (Fig. 4b) reflected the elongation trends in both conditions. Elongation decreased with Cu content steeply before heat treatment [28] and slightly after heat treatment, from 11 to 8%. Similarly, the average 3NN distance of the Q phases lies in the 9 - 4 μm range in the heat-treated condition, while in the as-cast condition, the range was 3.5–1 μm (Fig. 4b). This correlates well with the significant drop in elongation in previous work [28].

3.3. *In-situ cyclic tests – 2D observations*

Table 4 shows the results of the in-situ cyclic tests belong to the low-cycle fatigue regime, as the samples survived 340–1500 cycles. The addition of Cu content did not determine the fatigue life of the samples, as the results are randomly distributed within this range.

Table 4
Summary of the in-situ cyclic tests on heat-treated CT samples.

Alloy	Sample	Cycles survived
Cu 0	A	800
	B	1500
	C	1253 (stopped for FIB milling)
Cu 0.5	A	690
	B	340
Cu 1.5	A	740
	B	1065
Cu 3.0	A	730
	B	925
	C	640 (stopped for FIB milling)

3.3.1. *Crack initiation*

The fatigue crack initiation in heat-treated conditions of a hypo-eutectic Al–Si cast alloy results from micro-scale defects or discontinuities at the surface and subsurface levels. A 2D perspective indicated that the crack initiation appeared in the primary dendrite in the Cu-free alloy (Fig. 6a–b and highlighted in Fig. 7a); Cu additions moved it to the interdendritic regions (Fig. 6c–h). Fig. 6g–h shows that the nucleation sites were observed at the grain boundaries (dashed yellow lines, over-imposed from the EBSD maps) in Alloy Cu 3.0. Fig. 6h shows two cracks that originated from the same point and follow the grain boundaries. On the other hand, Fig. 6a–f shows cracks in the grain centre in all of the investigated specimens with lower Cu concentrations. From observing the polished surfaces, it can be concluded that crack nucleation occurred in the grain for Cu contents up to 1.5 wt% and aligned with the grain boundary for Alloy Cu 3.0. Moreover, defects or discontinuities at the sub-micron scale, such as precipitates, that can act as initiation sites were not observed in this work and need different investigative

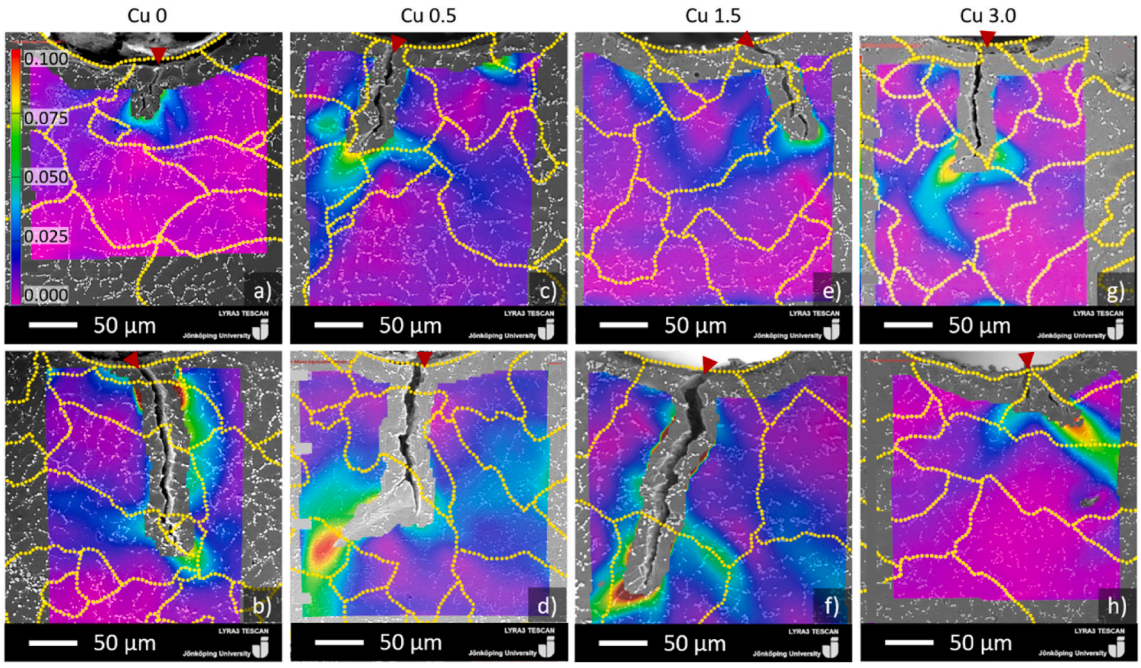

Fig. 6. Crack propagation in all heat-treated alloys combining EBSD and Digital Image Correlation (DIC): a-b) Alloy Cu 0; c-d) Alloy Cu 0.5; e-f) Alloy Cu 1.5; g-h) Alloy Cu 3.0. The dashed yellow lines represent grain boundaries, super-imposed from EBSD, and red arrows point to the initiation sites. The colour bar represents the von Mises equivalent strain and is valid for all the frames. (For interpretation of the references to colour in this figure legend, the reader is referred to the Web version of this article.)

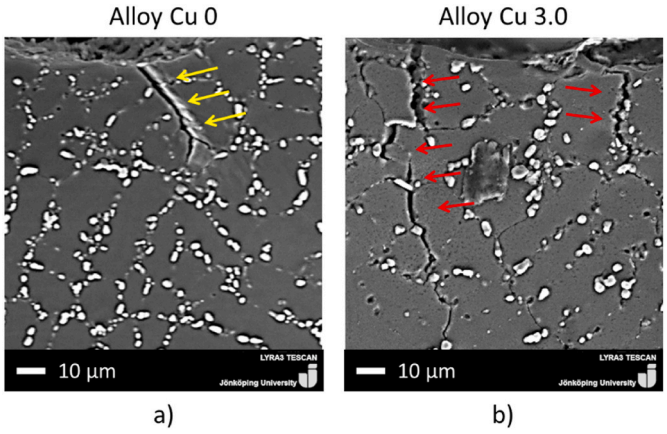

Fig. 7. Examples of crack path: a) trans-dendritic in Alloy Cu 0, pointed by yellow arrows; b) inter-dendritic in Alloy Cu 3.0, pointed by red arrows. (For interpretation of the references to colour in this figure legend, the reader is referred to the Web version of this article.)

approaches.

3.3.2. Crack propagation

Crack propagation is generally expected to follow the least resistance path, offered by weak or damaged microstructural features ahead of the crack tip. The EBSD maps generated were super-imposed on the SEM micrograph, and the dashed yellow lines in Fig. 6 represent the grain boundaries.

In Alloy Cu 0 (Fig. 6b), the crack propagated along trans-granular paths for the first 150 µm in the FOV, then continued following the grain boundaries. The propagation followed a mixed path that crossed the dendrite arms and followed the eutectic Si particles.

Crack propagation shifted slightly to the interdendritic regions with the Cu addition of 0.5 wt% (Fig. 6c–d). This shift occurred due to the enhanced strength in α-Al matrix strength due to the retained Cu, evidenced by WDS measurements in Fig. 3b and hardness values in Fig. 5d. The DIC results for Alloy Cu 0.5 highlighted that increment of strain concentration occurred at the grain boundaries. However, the main propagation path was trans-granular.

In Alloy Cu 1.5 (Fig. 6e–f), the propagation is mainly trans-granular with some intergranular segments, despite the increased strain concentration at the grain boundaries.

Concerning Alloy Cu 3.0 (Fig. 6g–h), the 2D perspective showed that crack growth tended to follow the grain boundaries. Fig. 6g shows that the propagation later continued across the grains. In Fig. 6h, two cracks are propagated under the dashed yellow lines along the grain boundaries and determined the higher strain highlighted by the DIC.

The crack propagation appears to be mixed on the surface, most as trans-granular and some inter-granular paths were present in all alloys. DIC in Fig. 6 highlighted that grain boundaries could determine localised strain, and it can ease crack propagation by determining the occurrence of intergranular segments (Fig. 6h). More often, the highest strain path is not determined by the grain boundaries (Fig. 6d). Other works [37,38] concluded that grain boundaries serve to distribute deformation in the microstructure, aligning with what is observed about crack propagation in Fig. 6. Han et al. [38] investigated short fatigue crack growth in Al–7Si-0.4 Mg alloy and reported that the grain boundaries deaccelerate crack propagation by a shielding effect. Nevertheless, the role of grain boundaries is based only on limited 2D data in the present study, and more investigation is required for a comprehensive assessment.

The increased Cu content in the α-Al matrix, as precipitates, provide significant obstacles for the dislocation movement, as shown by Roy et al. [17] and Saito et al. [14]. This phenomenon transfers the propagation from the α-Al matrix in Alloy Cu 0 (yellow arrows in Fig. 7a) to the eutectic regions in Alloy Cu 3.0 (red arrows in Fig. 7b), with an increased number of damaged Si particles and Q phases. This phenomenon is related to the primary matrix strengthening observed previously (Fig. 5d) in the present work. Similar behaviour was observed in Alloy Cu 1.5, whereas the propagation changed from trans-dendritic to inter-dendritic.

Another significant change was the presence of multiple secondary cracks appearing in the FOV during cyclic loading, indicated by arrows in Fig. 8. These secondary cracks followed the Si particles and Q phases (Fig. 8a) and opened up as cyclic loading continued (Fig. 8b). The cracks followed the interdendritic regions and connected the secondary phases due to the reduced 3NN distance between the Q phases, as shown in Fig. 8c and d.

Secondary cracks were not evident in the FOV of Alloy Cu 0 and Cu 0.5. Moreover, some cracks were detected in Cu 1.5, and many secondary cracks developed in Alloy Cu 3.0 (Fig. 8). The α-Al matrix strength governed the stress concentrations in the alloy and, consequently, the propagation behaviour. Inter-dendritic secondary cracks developed along the lateral dendrite tips with increasing α-Al matrix strength. The material within the FOV was involved in dissipating the deformation that resulted from the cyclic loading, not only the primary crack but also the secondary cracks in the interdendritic regions (Fig. 8c–d). This increasing trend of secondary crack development aligns well with the decreasing 3NN distance between Cu-based phases (Fig. 4b), which enabled the connection between small cracks.

The influence of the strengthened α-Al matrix on the evolution of the crack path can also be assessed with crack tortuosity. Fig. 9 shows that tortuosity varied within 1.1–1.2 for the heat-treated alloys, a more limited range than what found in previous work [28]. Given the constant values of AGS and SDAS for the alloys in all conditions, the evolution of tortuosity with the Cu content accords well with the elongation results in Fig. 5c.

In the heat-treated alloys, the constant crack tortuosity trend was related to a constant ductility trend. The values for tortuosity for Alloy Cu 1.5 were the same before [28] and after heat treatment, with a limited difference in elongation (Fig. 9).

In previous work [28], Alloy Cu 3.0 had a rapid failure without any previously detectable deformation. However, after heat treatment, the crack propagation was not sudden and could be followed in the FOV during in-situ cyclic loadings at all levels of Cu concentration. Furthermore, the improved elongation (Fig. 5c) coupled with the enhanced hardness of the primary α-Al matrix (Fig. 5d) compared to previous work [28] highlights that Cu-containing alloys benefit from an excellent balance between strength and ductility with heat treatment. With this condition, the damage is progressive during cyclic loading rather than sudden, as was previously reported [28].

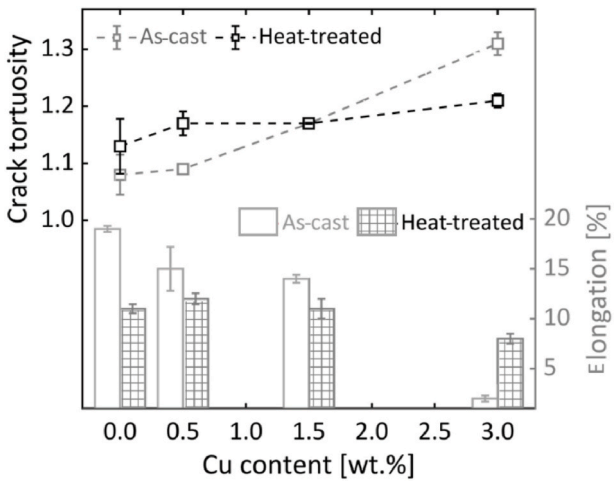

Fig. 9. Comparison of crack tortuosity and elongation trends in the as-cast and heat-treated conditions. The trend lines are meant to guide the eye. The as-cast values from previous work [28] are depicted for direct comparison.

3.4. *In-situ cyclic tests – 3D evaluations*

3.4.1. *FIB slicing*

The 3D evaluation using FIB slicing of the extreme conditions, Alloys Cu 0 and Cu 3.0, was performed to investigate the development of secondary cracks in Fig. 8. Fig. 10a and d shows the AOI (white rectangles) for the FIB sections investigated of Alloy Cu 0 (Fig. 6a) and Cu 3.0 (Fig. 6h). A 2D perspective showed that crack propagation stopped at the grain boundary during the cyclic testing of Alloy Cu 0. At the beginning of the FIB sections (Fig. 10b), no crack was visible in the thickness but was evident on the surface (white arrow). The bright phases in Section 1 (black arrows in Fig. 10b) are Fe-containing phases, as confirmed by EDS measurements. Moreover, investigating the sections moving toward the crack showed a limited amount of cracked or debonding phases. In Section 170 (Fig. 10c), a crack opened from the underlying volume (red arrows), indicating crack initiation below the surface.

As the Cu concentration increased to 3.2 wt% (Fig. 10d), multiple cracks were visible on the surface of the sample. The white arrow in Fig. 10e points to the surface crack, which extended to the material

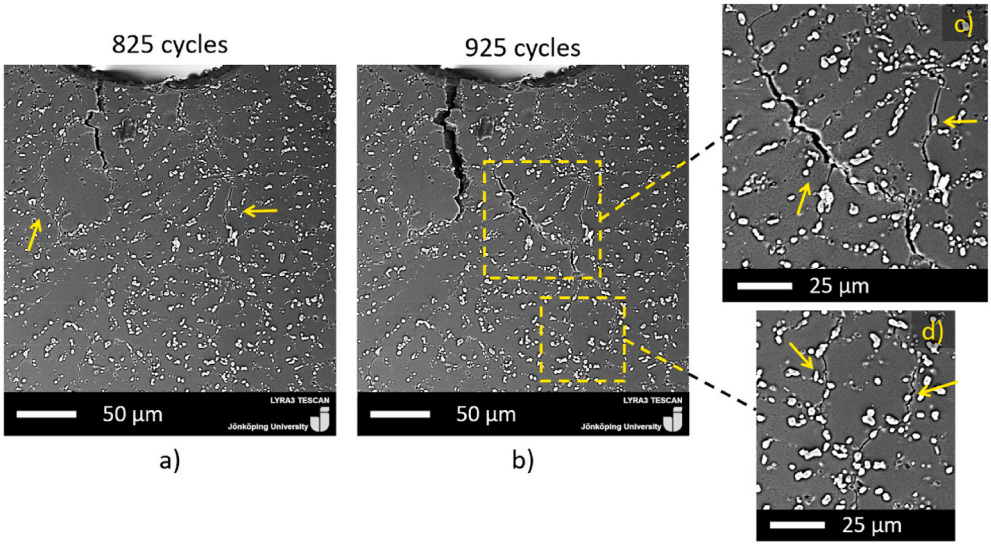

Fig. 8. Development of secondary cracks (indicated by yellow arrows) in heat-treated Alloy Cu 3.0: a) 825 cycles; b) 925 cycles; c-d) magnified micrographs of secondary cracks in (b). (For interpretation of the references to colour in this figure legend, the reader is referred to the Web version of this article.)

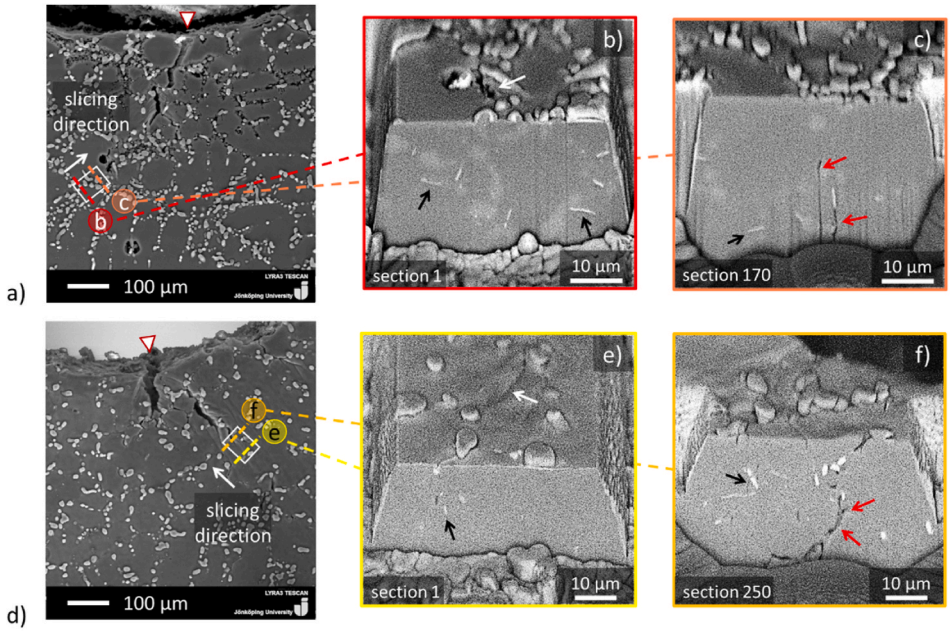

Fig. 10. FIB sections used to investigate the material around the crack in heat-treated alloys. a) Alloy Cu 0, test stopped at 1253 cycles; b) and c) show related sections; d) Alloy Cu 3.0, test stopped at 640 cycles; e) and f) show related sections. The black arrows point to Fe compounds, the white arrows point to superficial cracks, and the red arrows point to the crack coming from underneath. (For interpretation of the references to colour in this figure legend, the reader is referred to the Web version of this article.)

underneath. In the FIB sections, a significant amount of cracked and debonded phases was present ahead of the crack tip compared to Alloy Cu 0. Moreover, the sections toward the crack (Section 250 in Fig. 10f) clearly shows that the crack propagated from below (red arrows) in the Cu phases, which were close to each other 4 µm on average (Fig. 4b).

These insights on crack propagation from subsurface material also support the appearance of the secondary cracks visible in Fig. 8b. These might be the final parts of cracks that developed underneath, from coalescence between cracked particles, and ultimately reached the polished surface appearing as secondary cracks.

Fig. 11b and d shows the 3D reconstruction of the volume removed by FIB slicing, showing cracks as red and intermetallic phases as blue in the alloys. Moreover, the arrows in the 2D view Fig. 11a and c follow the same colour legend. Alloy Cu 0 (Fig. 11a) has few cracks in the investigated AOI, while Alloy Cu 3.0 (Fig. 11c) contains significantly more cracks. In Alloy Cu 0 (Fig. 11b), the crack appears from below, as visualised in Fig. 10c. In alloy Cu 3.0 (Fig. 11d), more connected microcracks are observed in the AOI. Furthermore, the 3D reconstruction confirms that cracks are frequently visible in connection with intermetallic phases, as previously observed in 2D slicing (Fig. 10f).

3.4.2. *Fracture surface analyses of CT samples*

Investigations of fracture surfaces showed that initiation sites were distributed along with the thickness of the CT samples. This outcome aligns with the FIB sections in Figs. 10 and 11, which showed cracks originating in the subsurface area. The supposed initiation points observed in the 2D view in Fig. 6a and h are a later stage of the crack propagation because of the triaxial stress state. The crack propagation zone (highlighted with the dashed yellow line in Fig. 12a and d) was distinct from the final fracture zone in the investigated alloys. Moreover, all of the samples show shear lips (solid yellow lines in Fig. 12a and d, showing Alloys Cu 0 and Cu 3.0) with significant height differences. Magnified views are depicted in Figs. 12c and f for Alloys Cu 0 and Cu 3.0, respectively. The fracture morphology of shear lips indicated a

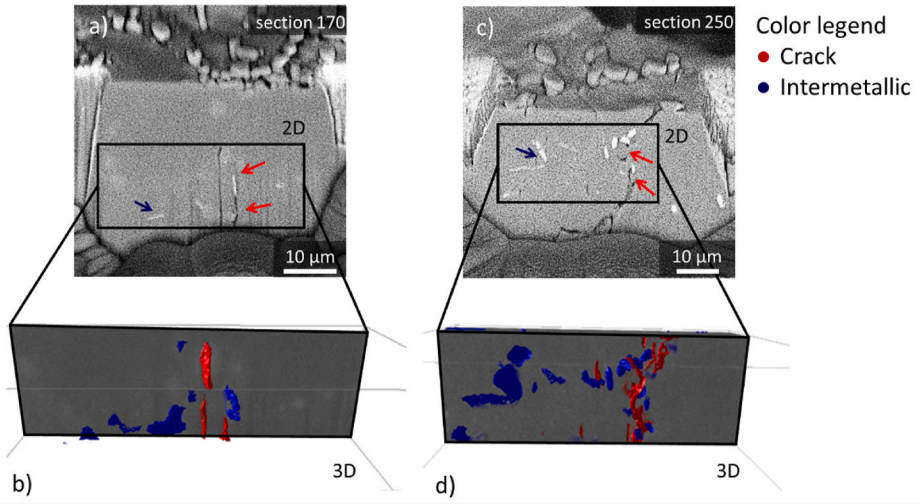

Fig. 11. 3D reconstruction of the FIB sections of the crack in heat-treated alloys. a) FIB section of Alloy Cu 0, test stopped at 1253 cycles, and b) related 3D reconstruction; c) FIB section in Alloy 3.0 Cu, test stopped at 640 cycles, and d) related 3D reconstruction. The red arrows show the cracks, and the blue arrows show the intermetallic phases. (For interpretation of the references to colour in this figure legend, the reader is referred to the Web version of this article.)

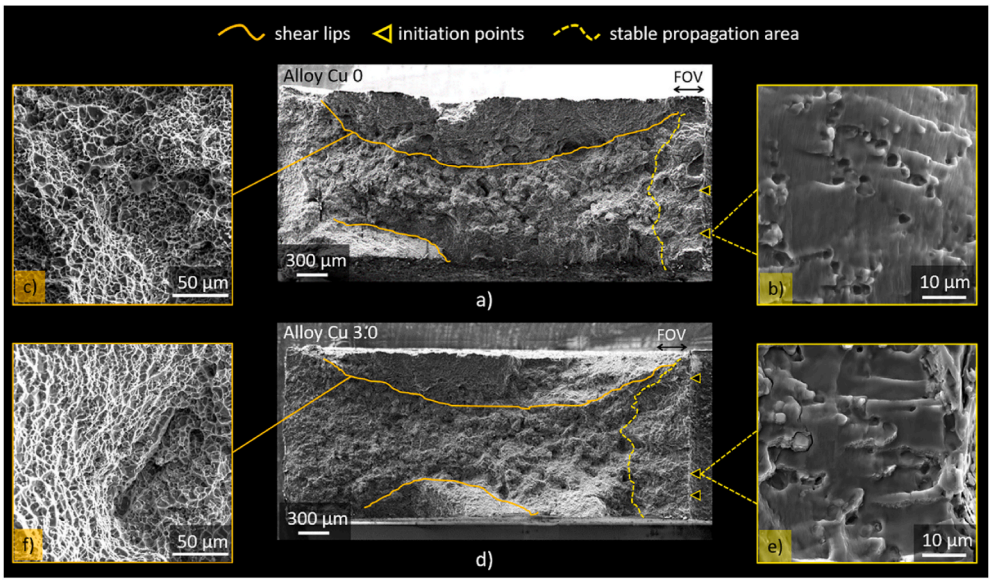

Fig. 12. Fracture surfaces of heat-treated Compact-Tension (CT) samples: a) Alloy Cu 0, b) and c) are magnified views of initiation points and shear lips, respectively, in a); d) Alloy Cu 3.0, e) and f) are magnified views of initiation points and shear lips, respectively, in d).

ductile behaviour, and similar dimples characterised the entire final failure zone in all of the alloys.

In Alloy Cu 0, the fracture surface at the notch showed that initiation started at two locations, each with a different crack propagation orientation. The magnified view of the propagation zone (Fig. 12b) shows Si particles rising from the surface. This feature suggests that the Si particles were debonded and pulled out from the α-Al matrix during crack propagation.

In Alloy Cu 3.0, the initiation started at multiple points, and several cracks appeared in the propagation zone. In the enlarged view (Fig. 12e), a mixture of debonded Si particles and cracking around particles are visible; these occurred due to the enhanced strength of the α-Al matrix. The difference from previous work [28] was significant for the alloy with 3.2 wt% Cu, in which a rapid failure occurred due to the presence of a significantly greater quantity of Q and θ phases. However, the reduction in the number of Cu-rich particles in Alloy Cu 3.0 after heat treatment changed the propagation behaviour of the alloy, and the crack path was visible in Fig. 6g–h.

In summary, the presented results show the critical role of Cu in Al–Si–Mg cast alloys to determine both crack initiation and propagation. The addition of Cu above 1.5 wt% transfers the propagation from the primary α-Al matrix to the eutectic regions because of the complex interaction between the strengthened α-Al matrix and intermetallic phases.

4. Concluding remarks

This study investigated the influence of microstructural features on tensile properties and crack development during cyclic loading in heat-treated Al–7Si–Mg alloys with different Cu additions. The following conclusions can be drawn:

- The limited variation of Si particles after heat treatment, in terms of morphology and three-nearest-neighbour distance, shown that mechanical properties are affected by Cu-based phases and primary matrix to a great extent.
- The addition of Cu resulted in a continuous improvement in YS and UTS up to 327 and 418 MPa, respectively. The parallel decrease in elongation was limited, from 11% to 8%, while crack tortuosity in CT samples followed the opposite trend with Cu additions.
- Crack initiation occurred at multiple sites in the thicknesses of the samples, as clarified by FIB sections and fracture surfaces. From the 2D perspective, crack propagation appeared mostly trans-granular in all the materials. However, the crack moved from trans-dendritic to inter-dendritic as the Cu content increased.
- The primary α-Al matrix was the most significant feature to influence crack propagation, as the strengthening effect of Cu influenced the development of inter-dendritic secondary cracks. These formed from the coalescence of small cracks that originated in the Si particles and intermetallic phases.

The 2D observations were interpreted differently after the three-dimensional insights provided by FIB sections and fracture surfaces. This study provided a deeper understanding of the relationship between crack development and microstructural features, useful for optimised structural components. Future studies will investigate the variation of other microstructural features that influence the mechanical response.

CRediT authorship contribution statement

Toni Bogdanoff: Investigation, Data curation, Writing – original draft. **Lucia Lattanzi:** Investigation, Data curation, Writing – original draft. **Mattia Merlin:** Supervision, Writing – review & editing. **Ehsan Ghassemali:** Visualization, Methodology, Writing – review & editing. **Anders E.W. Jarfors:** Supervision, Writing – review & editing. **Salem Seifeddine:** Conceptualization, Supervision, Resources, Writing – review & editing, All the authors contributed to and read the final manuscript.

Declaration of competing interest

The authors declare that they have no known competing financial interests or personal relationships that could have appeared to influence the work reported in this paper.

Acknowledgements

The authors gratefully acknowledge Mr. Riccardo Castiglieri for help in performing part of the experimental work.

Appendix ASupplementary data

Supplementary data to this article can be found online at https://doi.org/10.1016/j.msea.2021.141930.

Funding

This research did not receive any specific grant from funding agencies in the public, commercial, or not-for-profit sectors.

Data availability

The data that support the findings of this study are available from the.

References

[1] A.C. Serrenho, J.B. Norman, J.M. Allwood, The impact of reducing car weight on global emissions: the future fleet in Great Britain, Phil. Trans. R. Soc. A (2017) 20160364.
[2] N. Hooftman, M. Messagie, J. Van Mierlo, T. Coosemans, A review of the European passenger car regulations – real driving emissions vs local air quality, Renew. Sustain. Energy Rev. 86 (2018) 1–21.
[3] Hydro papers, E-mobility 2020 – Materials Selection for a More Sustainable Automotive Future, May 2020, pp. 1–24.
[4] R. Taghiabadi, A. Fayegh, A. Pakbin, M. Nazari, M. Ghoncheh, Quality index and hot tearing susceptibility of Al–7Si–0.35 Mg–xCu alloys, Trans. Nonferrous Metals Soc. China 28 (7) (2018) 1275–1286.
[5] S. Seifeddine, E. Sjölander, T. Bogdanoff, On the role of copper and cooling rates on the microstructure, defect formations and mechanical properties of Al-Si-Mg alloys, Mater. Sci. Appl. 4 (2013) 171–178.
[6] S. Shabestari, H. Moemeni, Effect of copper and solidification conditions on the microstructure and mechanical properties of Al–Si–Mg alloys, J. Mater. Process. Technol. 153 (2004) 193–198.
[7] C. Caceres, M. Djurdjevic, T. Stockwell, J. Sokolowski, The effect of Cu content on the level of microporosity in Al-Si-Cu-Mg casting alloys, Scripta Mater. 40 (5) (1999) 631–637.
[8] L. Ceschini, S. Messieri, A. Morri, S. Seifeddine, S. Toschi, M. Zamani, Effect of Cu addition on overaging behaviour, room and high temperature tensile and fatigue properties of A357 alloy, Trans. Nonferrous Metals Soc. China 30 (2020) 2861–2878.
[9] E. Cerri, M.T. Di Giovanni, E. Ghio, A study of intermetallic phase stability in Al-Si-Mg casting alloy: the role of Cu additions, Metallurgia Italiana 112 (7–8) (2020) 37–47.
[10] J. Baskaran, P. Raghuvaran, S. Ashwin, Experimental investigation on the effect of microstructure modifiers and heat treatment influence on A356 alloy, Mater. Today: Proceedings 37–2 (2021) 3007–3010.
[11] S. Beroual, Z. Boumerzoug, P. Paillard, Y. Borjon-Piron, Effects of heat treatment and addition of small amounts of Cu and Mg on the microstructure and mechanical properties of Al-Si-Cu and Al-Si-Mg cast alloys, J. Alloys Compd. 784 (2019) 1026–1035.
[12] M.T. Di Giovanni, E.A. Mørtsell, T. Saito, S. Akhtar, M. Di Sabatino, Y. Li, E. Cerri, Influence of Cu addition on the heat treatment response of A356 foundry alloy, Materials Today Communications 19 (2019) 342–348.
[13] E.A. Mørtsell, F. Qian, C.D. Marioara, Y. Li, Precipitation in an A356 foundry alloy with Cu additions-A transmission electron microscopy study, J. Alloys Compd. 785 (2019) 1106–1114.
[14] T. Saito, E.A. Mørtsell, S. Wenner, C.D. Marioara, S.J. Andersen, J. Friis, K. Matsuda, R. Holmestad, Atomic structures of precipitates in Al–Mg–Si alloys with small additions of other elements, Adv. Eng. Mater. 20 (7) (2018) 1800125.
[15] Y. Zheng, W. Xiao, S. Ge, W. Zhao, S. Hanada, C. Ma, Effects of Cu content and Cu/Mg ratio on the microstructure and mechanical properties of Al–Si–Cu–Mg alloys, J. Alloys Compd. 649 (2015) 291–296.
[16] C. Caceres, I.L. Svensson, J. Taylor, Strength-ductility behaviour of Al-Si-Cu-Mg casting alloys in T6 temper, Int. J. Cast Metals Res. 15 (5) (2003) 531–543.
[17] S. Roy, L.F. Allard, A. Rodriguez, T.R. Watkins, A. Shyam, Comparative evaluation of cast aluminum alloys for automotive cylinder heads: Part I—microstructure evolution, Metall. Mater. Trans. (2017) 1–14.
[18] S. Roy, L.F. Allard, A. Rodriguez, W.D. Porter, A. Shyam, Comparative evaluation of cast aluminum alloys for automotive cylinder heads: Part II—mechanical and thermal properties, Metall. Mater. Trans. 48 (5) (2017) 2543–2562.
[19] E. Sjölander, S. Seifeddine, The heat treatment of Al–Si–Cu–Mg casting alloys, J. Mater. Process. Technol. 210 (10) (2010) 1249–1259.
[20] K.S. Chan, P. Jones, Q. Wang, Fatigue crack growth and fracture paths in sand cast B319 and A356 aluminum alloys, Mater. Sci. Eng., A 341 (1–2) (2003) 18–34.
[21] D.A. Lados, D. Apelian, P.E. Jones, J.F. Major, Microstructural mechanisms controlling fatigue crack growth in Al–Si–Mg cast alloys, Mater. Sci. Eng., A 468 (2007) 237–245.
[22] D.A. Lados, D. Apelian, Fatigue crack growth characteristics in cast Al–Si–Mg alloys: Part I. Effect of processing conditions and microstructure, Mater. Sci. Eng., A 385 (1–2) (2004) 200–211.
[23] D.A. Lados, D. Apelian, L. Wang, Solution treatment effects on microstructure and mechanical properties of Al-(1 to 13 pct) Si-Mg cast alloys, Metall. Mater. Trans. B 42 (1) (2011) 171–180.
[24] D. Tomazincic, M. Borovinsek, Z. Ren, J. Klemenc, Improved prediction of low-cycle fatigue life for high-pressure die-cast aluminium alloy AlSi9Cu3 with significant porosity, Int. J. Fatig. 144 (2021) 106061.
[25] J. Hirsch, Automotive trends in aluminium - the European perspective, Mater. Forum 28 (2004) 15–23.
[26] G.K. Sigworth, R.J. Donahue, The metallurgy of Aluminum alloys for structural high-pressure die castings, Int. J. Metalcast. 15 (3) (2020) 1031–1046.
[27] T. Lu, J. Wu, Y. Pan, S. Tao, Y. Chen, Optimising the tensile properties of Al-11Si-0.3Mg alloys: role of Cu addition, J. Alloys Compd. 631 (2015) 276–282.
[28] T. Bogdanoff, L. Lattanzi, M. Merlin, E. Ghassemali, S. Seifeddine, The Influence of Copper Addition on Crack Initiation and Propagation in an Al-Si-Mg Alloy during Cyclic Testing, Materialia, 2020, p. 100787.
[29] E. Sjölander, S. Seifeddine, Artificial ageing of Al–Si–Cu–Mg casting alloys, Mater. Sci. Eng., A 528 (24) (2011) 7402–7409.
[30] J.J. Friel, Practical Guide to Image Analysis, ASM international, 2000.
[31] E. Vandersluis, C. Ravindran, Comparison of measurement methods for secondary dendrite arm spacing, Metallogr. Microstruct. Anal. 6 (2017) 89–94, https://doi.org/10.1007/s13632-016-0331-8.
[32] K.A. Kasvayee, E. Ghassemali, K. Salomonsson, S. Sujakhu, S. Castagne, A. E. Jarfors, Microstructural strain mapping during in-situ cyclic testing of ductile iron, Mater. Char. 140 (2018) 333–339.
[33] X. Wang, J. Embury, W. Poole, S. Esmaeili, D. Lloyd, Precipitation strengthening of the aluminum alloy AA6111, Metall. Mater. Trans. 34 (12) (2003) 2913–2924.
[34] S. Toschi, Optimisation of A354 Al-Si-Cu-Mg alloy heat treatment: effect on microstructure, hardness, and tensile properties of peak aged and overaged alloy, Metals 8 (11) (2018) 961.
[35] E. Sjölander, S. Seifeddine, Optimisation of solution treatment of cast Al-7Si-0.3 Mg and Al-8Si-3Cu-0.5 Mg alloys, Metall. Mater. Trans. 45 (4) (2014) 1916–1927.
[36] Y. Han, A. Samuel, F. Samuel, S. Valtierra, H. Doty, 08-014 effect of solution heat treatment type on the dissolution of copper phases in Al-Si-Cu-Mg type Alloys, Trans. Am. Foundrymen's Soc. 116 (2008) 79.
[37] A.C. Magee, L. Ladani, Representation of a microstructure with bimodal grain size distribution through crystal plasticity and cohesive interface modelling, Mech. Mater. 82 (2015) 1–12.
[38] S.W. Han, S. Kumai, A. Sato, Effects of solidification structure on short fatigue crack growth in Al-7%Si-0.4%Mg alloy castings, Mater. Sci. Eng. 332 (2002) 56–63.